Eur Biophys J
DOI 10.1007/s00249-017-1207-9

ORIGINAL ARTICLE

EBSA
Biophysics in Europe

Characterization of microtubule buckling in living cells

Carla Pallavicini[1] · Alejandro Monastra[2,4] · Nicolás González Bardeci[3,4] · Diana Wetzler[3,4] · Valeria Levi[3,4] · Luciana Bruno[1,4]

Received: 22 December 2016 / Revised: 15 March 2017 / Accepted: 3 April 2017

Abstract Microtubules are filamentous biopolymers involved in essential biological processes. They form key structures in eukaryotic cells, and thus it is very important to determine the mechanisms involved in the formation and maintenance of the microtubule network. Microtubule bucklings are transient and localized events commonly observed in living cells and characterized by a fast bending and its posterior relaxation. Active forces provided by molecular motors have been indicated as responsible for most of these rapid deformations. However, the factors that control the shape amplitude and the time scales of the rising and release stages remain unexplored. In this work, we study microtubule buckling in living cells using *Xenopus laevis* melanophores as a model system. We tracked single fluorescent microtubules from high temporal resolution (0.3–2 s) confocal movies. We recovered the center coordinates of the filaments with 10-nm precision and analyzed the amplitude of the deformation as a function of time. Using numerical simulations, we explored different force mechanisms resulting in microtubule bending. The simulated events reproduce many features observed for microtubules, suggesting that a mechanistic model captures the essential processes underlying microtubule buckling. Also, we studied the interplay between actively transported vesicles and the microtubule network using a two-color technique. Our results suggest that microtubules may affect transport indirectly besides serving as tracks of motor-driven organelles. For example, they could obstruct organelles at microtubule intersections or push them during filament mechanical relaxation.

Keywords Microtubules · Buckling · Active forces · Living cells · Filament tracking · Fluorescence microscopy

Introduction

Microtubules (MTs), together with actin and intermediate filaments, constitute the cytoskeleton that is essential for diverse biological processes ranging from mitosis (Walczak and Heald 2008), distribution of cellular compartments (Fletcher and Mullins 2010) and cargo transport (Howard 2009) to ciliary and flagellar motility (Nicastro et al. 2006). These biological processes require a microtubule network that responds to extra- or intracellular stimuli by modifying the distribution, lengths and curvatures of filaments (Gardel et al. 2008; Paluch et al. 2015).

Microtubule lengths are finely tuned by controlled cycles of polymerization and depolymerization (Dogterom and Yurke 1997; Akhmanova and Steinmetz 2015). These growing and shrinking cycles also affect the in vivo curvatures of microtubules since the overcrowded milieu

Electronic supplementary material The online version of this article (doi:10.1007/s00249-017-1207-9) contains supplementary material, which is available to authorized users.

✉ Luciana Bruno
lbruno@df.uba.ar

1 Departamento de Física, Facultad de Ciencias Exactas y Naturales, Universidad de Buenos Aires, Pabellón 1, Ciudad Universitaria, 1428 Buenos Aires, Argentina

2 Instituto de Ciencias, Universidad Nacional de General Sarmiento, JM Gutiérrez 1150, Los Polvorines, 1613 Buenos Aires, Argentina

3 Departamento de Química Biológica, Facultad de Ciencias Exactas y Naturales, Universidad de Buenos Aires, Pabellón 2, Ciudad Universitaria, 1428 Buenos Aires, Argentina

4 Consejo Nacional de Investigaciones Científicas y Técnicas, Buenos Aires, Argentina

Published online: 19 April 2017

presents barriers to the microtubule growing tip (Brangwynne et al. 2007).

Curvatures of microtubules in living cells also rely on the direct or indirect action of molecular motors (Bicek et al. 2009; Shekhar et al. 2013; Wu et al. 2011; Kent et al. 2016) that exert piconewton forces to bend these rigid polymers characterized by an in vitro persistence length of ~3 mm (Gittes et al. 1993).

Although it is widely accepted that active forces are intimately involved in shaping the microtubule network, we still do not completely understand the mechanisms involved in the continuous remodeling of microtubule curvatures. Hence, studying buckling events may unveil how these forces regulate the cytoskeleton organization and contribute to its functions.

Here, we explore how local forces model microtubule shapes in living cells using *Xenopus laevis* melanophores as a model system. These relatively big (40-μm average diameter) and thin cells provide a quasi-2D geometry that facilitates tracking individual microtubules with nanometer precision (Pallavicini et al. 2014).

We focus our analysis on exploring bending events of microtubules; these events are widely observed in different cell lines and result in the formation of micrometer-sized buckles that relax after a few seconds (Brangwynne et al. 2006; Rauch et al. 2013; Kent et al. 2016). In addition, we run numerical simulations to model different active mechanisms proposed in the literature to cause microtubule bending in vivo (Bicek et al. 2009; Wu et al. 2011; Shekhar et al. 2013) and compare their predictions with our experimental observations. Finally, we studied the interplay between microtubule bending and organelle transport and found that physical encounters between vesicles and MTs also introduce buckling of these filaments.

Results

Forces and buckling: simulation of microtubule motion and bending

To explore the effect of local forces applied to a microtubule, we considered a discretized 1D semi-flexible filament immersed in a homogeneous medium with a viscosity similar to that reported for the cell cytoplasm (Yamada et al. 2000). We then applied forces of different directionality and magnitude to the filament and followed the evolution of the microtubule shape. A detailed description of the model and its implementation in the numerical simulations is available in the "Materials and methods" section and supplementary information files.

We analyzed two scenarios involving MT compression: a microtubule under constant load and a microtubule sliding at constant speed. These conditions are schematized in Fig. 1a, b. The first case accounts for the pushing exerted by an organelle or a cross-linker on the filament (Kulic et al. 2008), whereas the second represents the compression of the microtubule caused by a stepping motor (Gittes et al. 1993; Kent et al. 2016). Then, we considered the effect of applying a lateral force on an MT, such as those produced by myosin motors in a reconstituted actin cytoskeleton (Brangwynne et al. 2008).

Tangential loads

Tangential forces, i.e., forces applied in the MT longitudinal direction, have been proposed to account for many microtubule deformation processes such as sliding (Kulic et al. 2008; Bicek et al. 2009; Kent et al. 2016), pushing and pulling (Kimura and Onami 2005; Howard 2006) or the retrograde movement of the actin network in a growth cone (Rauch et al. 2013).

When a compressive load is applied at the ends of a thin beam, it bends provided the force is larger than the Euler force (F_c). This critical force depends on the mechanical and geometrical properties of the rod. For an isotropic and homogeneous filament (Howard 2001):

$$F_c = a\,\frac{EI}{L^2} \tag{1}$$

where EI and L are the flexural rigidity and the length of the filament, respectively, and a is a constant that depends on the specific boundary conditions. The existence of a critical force imposes a lower bound limit on the tangential forces required to buckle an MT.

As an example, Fig. 1a shows a 5-μm-sized microtubule, clamped at one end, while the other one is allowed to move only in the longitudinal direction. The main conclusions of this and the following sections can be generalized to other filament lengths or boundary conditions. Initially, the filament is barely bent (amplitude equal to 0.1 nm), and at time $t = 0$ a constant force $F > F_c$ in the tangential direction is applied at the moving end. As a consequence, the microtubule starts to bend: the amplitude of the deformation, A, begins to grow exponentially,

$$A(t) = A_0 e^{t/\tau} \tag{2}$$

with a characteristic time given by (Howard 2001):

$$\tau = \tau_0\,\frac{F_c}{F - F_c} \tag{3}$$

where

$$\tau_0 = \frac{c}{EI}\quad (\alpha\, L)^4 \tag{4}$$

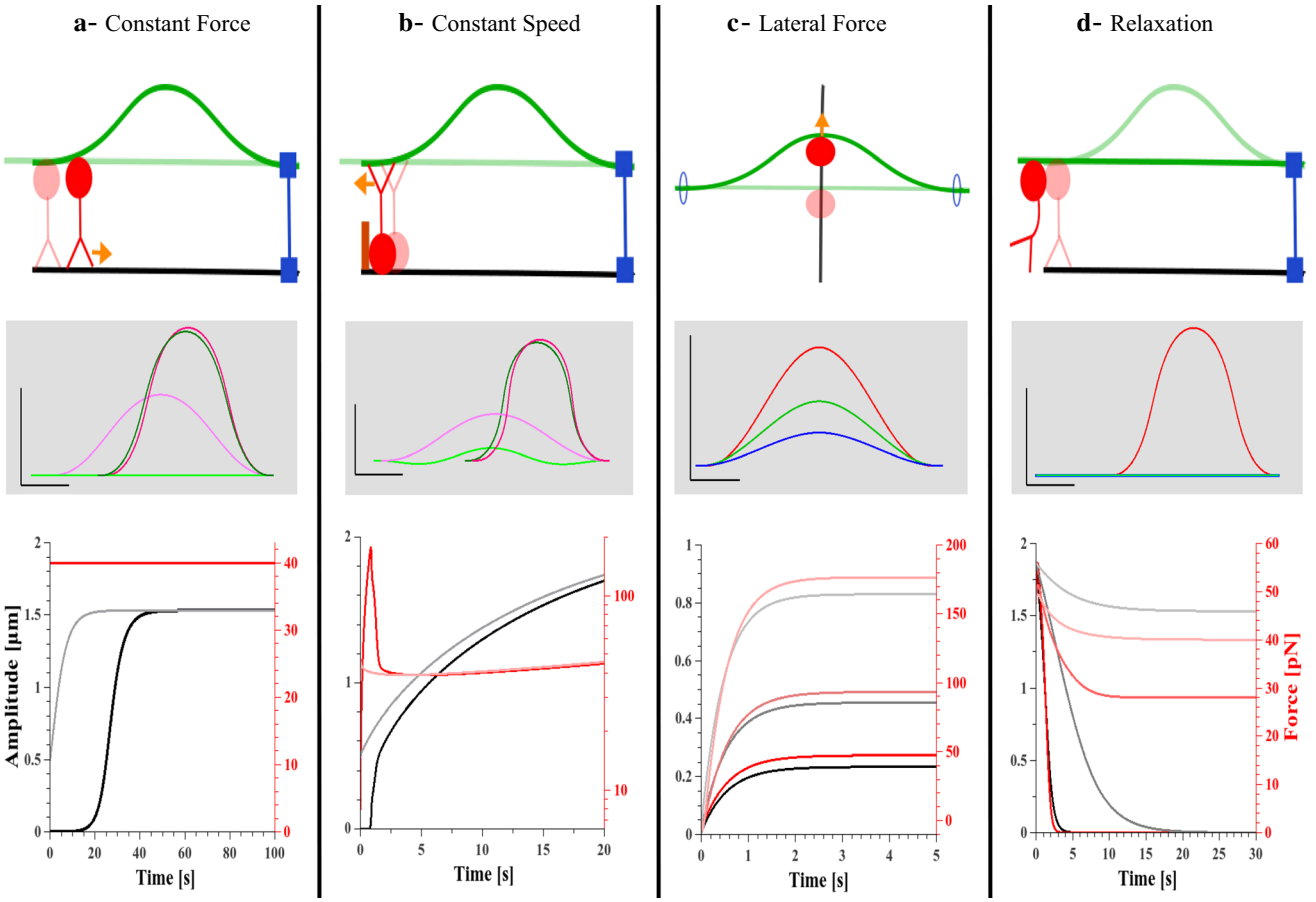

Fig. 1 Different motor force mechanisms that can produce MT buckling in living cells and their simulation results. The *upper panels* show a sketch of the biological assumptions. *Middle panels* represent the filament shapes at different times during the simulated buckling event for a $L = 5$ μm filament and clamped end conditions. *Lower panel* displays the amplitude and force time courses recovered for the different simulated scenarios. **a** Constant tangential load: a force $F = 40$ pN in the horizontal direction was applied at the moving end. Filament shapes at $t_1 = 2.5$ s (*light colors*) and $t_2 = 40$ s (*dark colors*) are shown. *Green* and *magenta filaments* correspond to simulations with initial amplitudes of 0.1 and 500 nm, respectively. The amplitude curves show different behaviors for $A_i = 0.1$ nm (*black*) and $A_i = 500$ nm (*gray*) at early times, but they converge to the same stationary shape. The force at the moving end during the time evolution is shown in *red*. **b** Constant speed compression. Filament is compressed at a constant velocity of 100 nm/s. Shapes for times: $t_1 = 1$ s and $t_2 = 20$ s are shown. Initial amplitudes and color codes as in **a**. Non-stationary shape is attained in this case. The force at the moving end is not constant. **c** Lateral force. In this condition, both ends are free to move horizontally but not vertically, and a constant pushing force is applied at the center of the filament in the vertical direction. The simulations were performed for $F_1 = 8$ pN, $F_2 = 16$ pN and $F_3 = 32$ p;, all initial conditions are straight ($A_i = 0$). MT shapes at $t = 2$ s when all amplitudes have stabilized. *Blue, green and red* correspond to F_1, F_2 and F_3, respectively. Time evolution of the amplitude (*black palette*) and force in the vertical direction felt at the tips (*red palette*) are shown. *Dark, mid and light colors* represent F_1, F_2 and F_3, respectively. **d** Relaxation of an MT segment after the release of the active force. An initially bent filament with amplitude 2 μm is released at $t = 0$. We simulated three scenarios: free release ($F_1 = 0$), partial force release to a value below critical buckling force ($F_2 = 28$ pN) and partial force release above the critical buckling force ($F_3 = 40$ pN). Final shapes of relaxed filaments are shown for F_1 (*blue*) and F_2 (*green*), and the filament relaxes to a zero amplitude condition. For F_3 (*red*), the filament does not relax completely. Time evolution of the amplitude (*black palette*) and the horizontal force (*red palette*) felt at the fixed (*right*) MT end. *Dark, mid and light colors* correspond to F_1, F_2 and F_3, respectively

is the characteristic relaxation time for $F = 0$. Here, c is the drag coefficient per unit length for the microtubule, which depends on the geometry of the filament as well as the viscosity of the environment, and α is a numerical factor depending on the boundary conditions.

However, after a short period of fast evolution, the amplitude growth slows down until, finally, it reaches an equilibrium plateau (Fig. 1a). The filament acquires a bent stationary shape, while the force at the fixed end equals F. The speed of the free end of the filament slows down accordingly. We also explored the effect of varying the initial amplitude and set it to 500 nm. For forces of equal magnitude, the stationary shape remains unchanged; the only observable difference is the amplitude evolution slope at early times (Fig. 1a).

To further buckle the filament, extra load has to be applied. In this case, the amplitude evolves toward the new stationary shape without displaying the initial exponential growth. However, if the extra load exceeds a threshold value the stationary buckling shape is not achieved and knotting of the filament occurs (Supplementary Fig. 7).

In Fig. 1b we consider a similar configuration as the one represented in Fig. 1a, but in this case the microtubule is compressed toward the fixed end at constant speed. This condition emulates a typical mechanism observed within cells (Kulic et al. 2008; Kent et al. 2016): when a motor protein is moving along an MT and encounters an obstacle, the motor steps on the filament without advancing. If the MT is pinned, this stepping results in a constant sliding of the filament toward the fixed end.

This simulation protocol introduces an interesting scenario. If the microtubule is initially straight, the filament explores transient undulating shapes as the compression proceeds (see Fig. 1b). Also, the system does not attain a stationary shape: the bending progresses until eventually the moving point passes over the fixed end, knotting the filament (Supplementary Fig. 7).

The force at the moving end, which would correspond to the motor stepping position, reveals the presence of a sharp increase for very short times associated with low values of the amplitude (Fig. 1b). The origin of this resistance to deformation can be attributed to an initial quasi-isoform compression of the filament, storing elastic energy. Consistently, the resistance force is reduced if the microtubule is pre-buckled. When the filament finally bends, the amplitude grows monotonously and the force relaxes to a lower non-zero value. We found that for very long filaments and/or low speeds, the amplitude develops a dependence with time given by:

$$A(t) \propto t^{1/2} \tag{5}$$

which comes from a geometrical constraint on the MT length.

Lateral force

It has been proposed that compressive loads cause microtubule bending (Gittes et al. 1996; Brangwynne et al. 2006; Kabir et al. 2015). However, forces in the transversal direction also produce MT buckling (Brangwynne et al. 2008) with characteristics that are almost indistinguishable from compressive ones, warning about the conclusions that can be extracted from experimental data. At this point, numerical simulations can help understand the effect of locally applied forces on microtubule deformation processes.

When a lateral force F is applied to a microtubule, the filament is dragged and deforms accordingly. Importantly, in this condition there is no critical force. Figure 1c shows a representation of a typical situation occurring in living cells: when a motor-driven cargo moving along an MT encounters another crossing filament, the latter is pushed laterally. In this case, the amplitude grows as:

$$A(t) = A_{\max}\,(1 - \mathrm{e}^{-t/\tau_0}) \tag{6}$$

with τ_0 given by Eq. (4). In agreement with the absence of critical force, the time scale of the process does not depend on the magnitude of the applied force. On the contrary, $A_{\max}$ varies linearly with F:

$$A_{\max} = \beta \frac{FL^3}{EI} \tag{7}$$

where β depends on the boundary conditions. When the force F is applied at the center of the filament and both ends are free $\beta = 1/128$, for clamped conditions $\beta = 1/192$ (see Supplementary material). For instance, for $L = 5$ μm and $F = 16$ pN the buckling amplitude is approximately 0.4 μm. In the free ends case, the force imposes a transversal effective drift to the filament, with a speed (Howard 2001):

$$V_{\text{drift}} = \frac{F}{c\,L} \tag{8}$$

which is of the order of a few nm/s for forces in the range of 1–10 pN and filaments of 5–10 μm length immersed in a very viscous environment (viscosity 10^3–10^4 times the viscosity of water). On the other hand, if the ends of the filament are prevented from displacing in the transversal direction, there is no global drift, which is the case of the simulations shown in Fig. 1c. It can be noticed in these cases that the buckling amplitude increases rapidly in early stages and then reaches a plateau. Drawing a biological analogy, we might say that the motor force pushing on the filament is balanced with the microtubule's resistance to bend.

Load release

The three scenarios described above can account for the trigger and development of filament buckling. Also, two of them predict a bent stationary shape. However, none of the mentioned mechanisms can explain the shape relaxation observed in MT buckling events. Since molecular motors produce the active forces responsible for MT buckling in living cells, their mechanical properties provide a plausible explanation for the bend termination.

In the cases shown in Fig. 1a, c, we argue that the force enhancement would increase the probability of motor detachment (Hendricks et al. 2012), consequently releasing the compression and relaxing the MT shape. On the other hand, the constant speed case is more intriguing since a rapid force enhancement appears, notably increasing the

probability of motor detachment before appreciable amplitude could be observed. However, if the resisting motor overcomes this initial large force without detaching, its probability of detachment will reduce since the resisting force decays after the bending (Fig. 1b). Although eventually the motor will detach, releasing the MT shape, this last scenario predicts the existence of buckling events with an extremely long duration for very robust motor teams.

Summarizing, when the load applied on the filament is released the filament shape relaxes, attaining a new equilibrium configuration given by F, a residual load (Fig. 1d). The amplitude decays exponentially with a characteristic time given by Eq. (3). If $F \simeq F_c$, the decay time diverges and the filament will relax very slowly. For lengths in the range 5–10 μm and typical viscosities 10^3–10^4 times that of water, the relaxation times range from 0.1 to 20 s (Howard 2001).

Boundary conditions and length dependence

Shapes and time scales during buckling events of MTs are not only governed by force load and direction. Boundary conditions can strongly affect the buckling shapes and dynamics (Jin and Ru 2013). From Eqs. (1) and (4), the critical force F_c, as well as the characteristic relaxation time τ_0, depends on the boundary condition through the coefficients a and α, respectively. We show this dependence in Fig. 2a where we plot the inverse of relaxation time as a function of the applied tangential force. We consider three cases: (i) free boundary conditions, where two equal and opposed forces are applied to each end, with both ends free to rotate (pivot); (ii) one fixed end, the force applied to the other moving end, both ends free to rotate; (iii) one fixed end, the force applied to the opposite end, both clamped. Cases (i) and (ii) have the same critical force $F_c = 8$ pN, with $a = \pi^2$, while case (iii) for clamped ends $F_c = 32$ pN with $a = 4\ \pi^2$. The recovered simulated shapes over time are illustrated in Supplementary Fig. 8a. We also simulated other force configurations with pivot boundary conditions; some examples are represented in the recovered shapes shown in Supplementary Fig. 8b, c.

The numerical simulations also reproduce the dependence of growing/decreasing time with applied force F given by Eq. (3). The relaxation time τ_0, which corresponds to no applied force, matches Eq. (4) with $\alpha = 2/3\pi$, $1/\pi$ and 0.2 for cases (i), (ii) and (iii), respectively.

Kabir et al. (2015) study the influence of length in the buckling of in vitro microtubules. Following their findings we analyze the length dependence for the clamped-clamped case (Fig. 2b). We compare simulations of 5- and 7-μm filaments. As expected, they follow the dependence on length from Eqs. (1) and (4). Increasing the length by

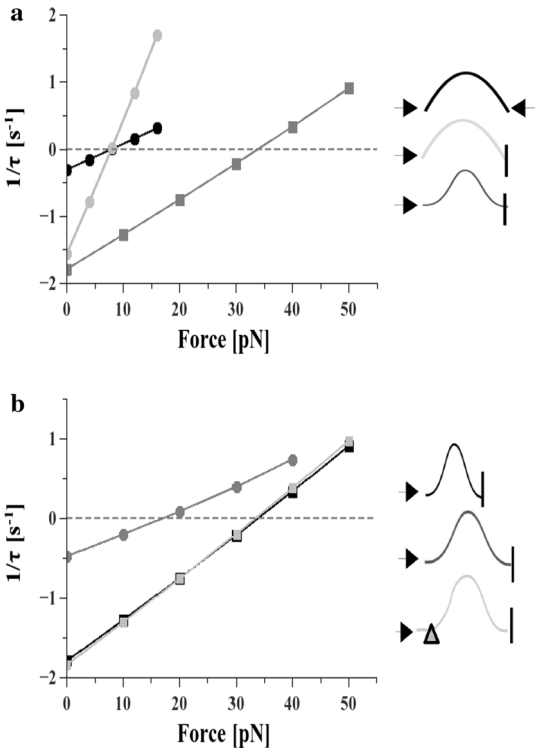

Fig. 2 Boundary conditions and length dependence. We performed simulations of microtubules with different lengths and boundary conditions and fitted the amplitude evolutions to Eq. (2). Here we compare the time-scale dependence with the applied force for constant tangential load cases. **a** Boundary conditions. Comparison of $1/\tau$ vs. force plots for 5-μm filaments with both ends free to rotate and moving symmetrically in the horizontal direction (*black circles*), both ends free to rotate with one fixed at a point and the other moving in the horizontal direction (*light gray circles*) and both ends clamped, one fixed and one mobile in the horizontal direction (*dark gray squares*). **b** Length dependence. Comparison of $1/\tau$ vs. force plots for filaments with clamped ends, with one fixed and one moving in the horizontal direction for: a 5-μm filament (*black squares*), 7-μm filament (*dark gray circles*) and 7-μm filament with the force applied 5 μm away from the fixed end (effective buckling length 5 μm) (*light gray squares*)

40% decreases the critical force by a half and increases the relaxation time by four.

We added a simulation of a 7 μm MT to this figure, where the force was applied at 2 μm from the free end, giving an effective bucking length of 5 μm. We observe that the critical force as well as the growing/decreasing times are practically the same as for a 5-μm filament, the contribution of the free part being marginal.

In all cases, when the applied force approaches the corresponding critical value, characteristic time τ diverges ($1/\tau \to 0$), the evolution being so slow that the MT seems stationary.

The numerical simulations performed so far provided an ample overview of buckling time courses under various force mechanisms. We found that semi-flexible filaments

present different buckling behaviors when subjected to forces applied in different configurations. Interestingly, we also noted that initial conditions can have a strong effect on the amplitude time evolution (Fig. 1a, b). The next step in this work is to observe and characterize buckling events in living cells.

Buckling events in *X. laevis* melanophores

We analyzed MT buckling events in *X. laevis* melanophores stably expressing EGFP-tagged XTP, a *Xenopus* homolog of tau protein, which binds to microtubules and therefore allows their visualization. Since this fluorescent protein binds and unbinds dynamically to microtubules, photobleaching is reduced, permitting the acquisition of longer movies. Microtubules were imaged using confocal microscopy with a temporal frequency of 0.1–4 Hz. The coordinates of the MT's central line positions were recovered with 10-nm precision using the semi-automated algorithm AFTER (Pallavicini et al. 2014). Figure 3a shows a representative image of the MT network. It can be observed that microtubules display long-range bends with mean curvatures $\kappa = (0.78 \pm 0.06)\ \mu m^{-1}$, corresponding to a radius of curvature $\rho = (1.3 \pm 0.1)\ \mu m$ ($n = 101$, mean $\pm$ standard error of the mean) (Supplementary Fig. 9). These values are in agreement with the findings of Rauch et al. (2013) who measured MT curvatures in the range of 0–2 μm^{-1} in NG108-15 neuronal cells. The arrowheads in Fig. 3a indicate some localized buckling, whose temporal evolution can be observed in movie ESM_1. This movie reveals a wonderful spectacle of sinuate filaments swaying within the cytoplasm. Figure 3b captures five snapshots of the evolution of the buckling event occurring on the highlighted filament. These are very common events; an average of 3.4 ± 0.7 events/min was observed ($n = 15$ cells, mean $\pm$ standard error).

To investigate the forces underlying buckling events, we treated cells with sodium azide—an ATP depleter—and registered the behavior of the microtubules under this condition (Movie ESM_2). Neither relaxation of bent MTs nor new bucklings arose, reinforcing previous results (Brangwynne et al. 2007) reporting that non-thermal forces originate these sudden and fast deformation events.

We also analyzed movies of cells treated with vinblastine, a drug that stabilizes MTs and thus arrests their polymerization and depolymerization dynamics. We found buckling events in the treated cells with a frequency of occurrence equal to 3.1 ± 1 events/min ($n = 12$ cells), which was similar to that observed in control cells (Supplementary Fig. 10). This result suggests that polymerization forces do not contribute significantly to MT buckling.

Spatial characterization of buckling events

To study the length scale of the buckling, we fitted the shape of the MT segment in the frame corresponding to the largest deformation to a Gaussian function (Fig. 4a). We associate the maximal amplitude A_{max} and σ to the size and spread of the buckling, respectively. The choice of a

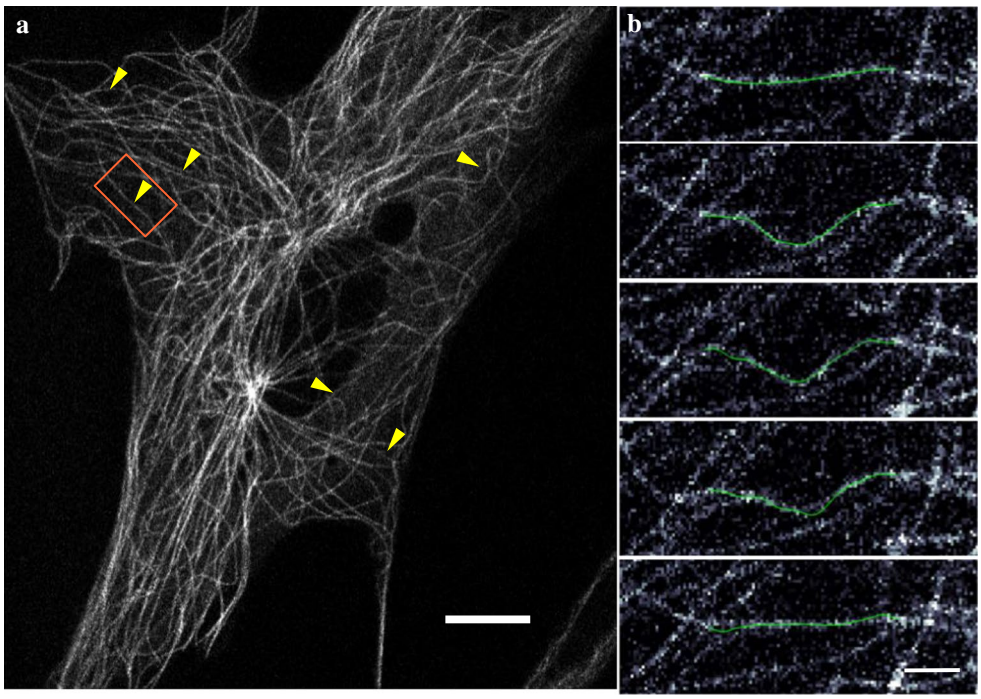

Fig. 3 The microtubule network is highly dynamic. Confocal images showing buckling and relaxation events. **a** Confocal image of GFP-labeled microtubules; the frame corresponds to a movie in which buckling and relaxations events are observed (*marked with yellow arrowheads*) *Scale bar* 10 μm. **b** Time evolution and tracking of the marked MT in **a**. Frames correspond to $t = 0$, 18, 53, 71 and 89 s, respectively. *Scale bar* 1 μm

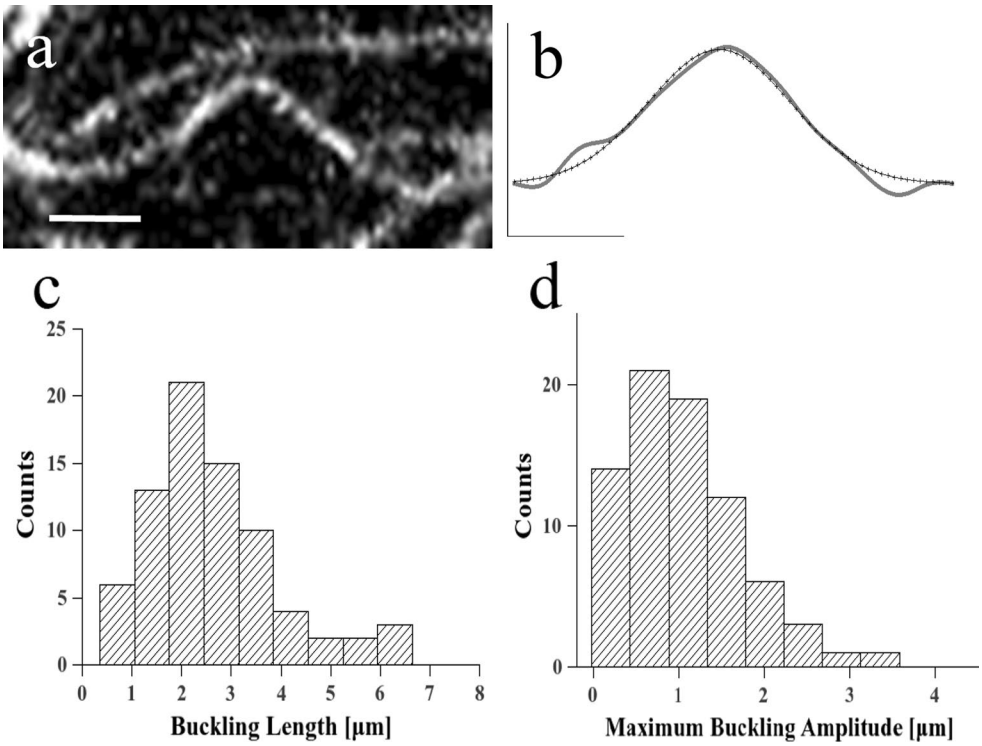

Fig. 4 Buckling analysis: shape. **a** Confocal image of the frame of maximum amplitude of the filament depicted in the time series of Fig. 2b. *Scale bar* 2 µm. **b** Tracked *xy* positions for the microtubule in **a** (*gray line*) and corresponding Gaussian fit (*black crosses*). *Scale bars* are both 2 µm. **c** Histogram of the recovered buckling characteristic lengths, defined as $L_c = 2\sigma$, where σ is obtained from the Gaussian fit in **b**. **d** Histogram of the measured maximum buckling amplitudes. For both histograms, the bin size was computed by Fridman-Diaconi's rule

Gaussian function to describe the deformation was arbitrary; similar results were obtained using a cosine function (not shown). We defined the characteristic length of the buckling as $L_c = 2\sigma$.

We found an average value of $L_c = (3.0 \pm 0.2)$ µm and $A_{max} = (1.3 \pm 0.08)$ µm ($n = 75$; mean ± standard error of the mean) (Fig. 4b, c). Similar values of L_c were reported for other systems such as cardiac rat myocytes, Cos7 cells (Brangwynne et al. 2006) and neuronal growth cones (Rauch et al. 2013). In those studies, the values of L_c were related to the ratio between the microtubule flexural rigidity and the elastic constant of the surrounding medium. Assuming reported values for the elasticity of the cytoplasm and flexural rigidity of the MTs, these authors obtained that compressive forces of the order of 100 pN are required to initiate a buckling event. However, we cannot rule out that the origin of this length scale stems from other factors such as physical obstacles acting as pinning points for the MTs (Kent et al. 2016; Jin and Ru 2013) or localized motor forces (Wu et al. 2011), resulting in lower values of the acting forces.

Bucklings are characterized by a burst in amplitude followed by a relaxation phase

To analyze the time course of MT buckling events, we recovered the coordinates of these microtubule segments in each frame (Fig. 3b) and computed the amplitude of the recovered shapes, as described in "Materials and methods." Typically, the amplitude followed three stages: baseline, growing and relaxation periods (Fig. 5a).

The buckling duration, defined as the period between the onset of the amplitude rise and the moment of maximal amplitude value, ranged from 1 to 200 s. The distribution could be well fitted by a power law (Fig. 5b) meaning that there is not a scale factor to set a characteristic duration of the events (Newman 2005). The finding of rare long events can also be explained considering the results obtained in the simulations of constant speed compression, as previously noticed. In that case, we found that the resisting force is not monotonous, but it decreases when the bending starts. We hypothesized that robust motor teams can persist for very long times attached to the MT and continue sliding the filament in this condition.

In views of the results obtained with the numerical simulations and in order to investigate the growing phase behavior of the amplitude, we considered the following ansatz (Howard 2001):

$$A = A_{eq} + \left[A_i - A_{eq}\right] e^{-(t-t_0)/\tau} \quad (9)$$

where A_i and A_{eq} are the baseline and maximum equilibrium amplitude, respectively, t_0 is the buckling onset time, and τ is the characteristic time of the growing stage given by Eq. (3). However, we noticed from the numerical simulations that the amplitude evolves as the square root of time (Eq. 4) if the speed of compression, instead of the force, is conserved.

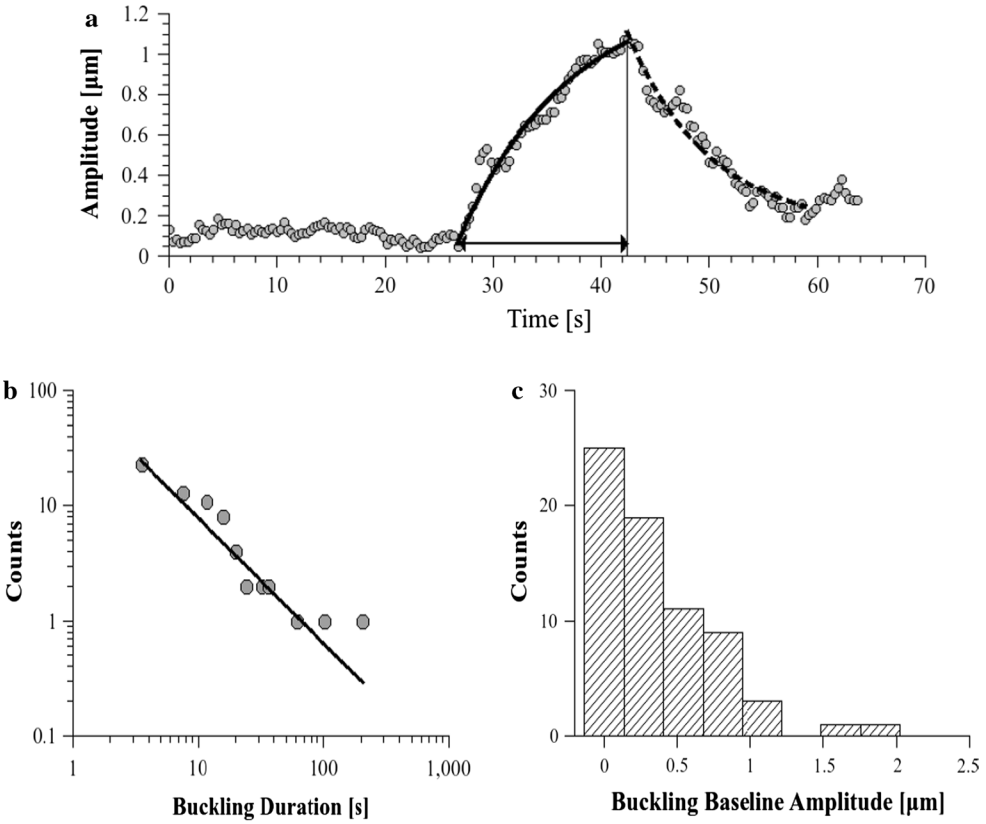

Fig. 5 Buckling analysis: fits and buckling characteristics. **a** Time series of measured amplitudes for an MT that undergoes a buckling and relaxation event (*gray circles*) with corresponding fits in the buckling (*solid black line*) and relaxation (*dashed black line*) time intervals. Both data sets were fitted to Eq. (9). The *vertical black line* indicates the maximum amplitude, and the horizontal, *double-headed arrow* illustrates the buckling duration. **b** Power law fit to the buckling duration histogram (measured data: *gray circles*; fitted curve: *black line*). Power law exponent: $\alpha = (-1.01 \pm 0.05)$. **c** Histogram of buckling baseline amplitude

First, we must select the data corresponding to the growing stage of the particular events from the complete time course. This procedure was performed by eye inspection, as suggested in Fig. 5a (see also "Materials and methods"). Once these data sets were determined, their time courses were first fitted using the expression given by Eq. (9).

In the first place, we noticed that the baseline amplitude was not negligible in most of the cases (Fig. 5c), and it ranged between 1 and 80% of the maximum amplitude of the corresponding buckling. Let us remark that the baseline amplitude reflects the pre-buckling curvature of the MT segment. As already mentioned, microtubules are rarely straight within cells but typically they are slightly bent (Brangwynne et al. 2007; Rauch et al. 2013) with curvatures in the range of 0–3 μm^{-1}. These curvatures correspond to bending amplitudes with a mean value of $\langle A \rangle = 0.45 \pm 0.07$ μm ($n = 101$, mean ± standard error of the mean) (Supplementary Fig. 9), in agreement with the data shown in Fig. 5c. The pre-buckling curvature facilitates buckling since little extra force is required to further deform the filament (Howard 2001; Rauch et al. 2013).

Then, from a total of 72 analyzed buckling amplitude time courses, we found that only 12.5% (9/72) of the data could be fitted by a positive exponent (Eq. 2), while 55.6% (40/72) agreed better with a negative exponent (Eq. 9) (Supplementary Fig. 12). Concerning this last data set presenting concave down behavior, 5 of the 40 events could also be satisfactorily fitted by the expression given by Eq. (5). However, because of the experimental uncertainties, it was not possible to choose which model gave the most accurate description. The remaining 32% (23/72) of the data, although developing a growing behavior, could not be satisfactorily fitted with any of the proposed models.

Regarding the first subset of buckling events that presented a concave up-growing regime and based on the numerical simulation results obtained previously, we wondered if this behavior could be explained considering that the microtubule was initially straight or had a very small curvature. Thus, we looked at the baseline amplitudes (Fig. 5c) obtained for these events and found that all the values are in the range of 60–360 nm. To determine whether these small amplitudes could be observed by chance, we used a bootstrapping procedure (Chernick 2007) to compute the probability of obtaining values of $A_i < 360$ nm when sampling $n = 9$ random events taken from the distribution displayed in Fig. 5c. We found that this probability was smaller than 3%, and thus we cannot rule out that the observation of an exponential growth is due to the initially almost straight microtubule.

Let us remark that the proposed scenarios in the simulations represent very ideal conditions (e.g., constant longitudinal force or constant sliding), while the situation within

living cells is richer, and thus it is expected that mixed conditions would be present in the real system. Despite this, we found that this simple model can account for many aspects of the buckling evolution, such as the observed amplitude time courses with their typical length and temporal scales.

After reaching the maximal amplitude, microtubules relax to a quasi-stationary shape. This relaxation can be interpreted as a load release process and could be well fitted by an exponential decay behavior given by Eq. (9). In this case, t_0 and A_i correspond to the time and value of the maximum amplitude, respectively, and A_{eq} is the amplitude at long times. The distribution of τ was exponential, resulting in a characteristic time of the decays of 11.5 ± 1.0 s. These values are in agreement with the ones in the range 0.64–44 s predicted for the free relaxation of microtubules with lengths between 5 and 15 μm and viscosity 5000 times that of water (Howard 2001).

On the other hand, the post-relaxation stationary amplitudes were not significantly different from the pre-buckling ones (Fig. 5c) as assessed by a Kolmogorov-Smirnov test (p value >0.78). This result suggests that microtubules within cells are intrinsically curved or they are pre-stressed.

In some cases, multiple events occur during the observation temporal window. These events concern single mode deformations of a microtubule occurring successively in time and do not refer to the multiple, simultaneous peaks observed in other works (Brangwynne et al. 2006; Jin and Ru 2013; Kabir et al. 2015) (Supplementary Fig. 10 and Supplementary movie ESM_3). Although these events were produced in almost identical conditions, i.e., the same MT segment is involved, and no substantial variations of the properties of the surrounding medium are expected, they displayed different amplitudes, sizes and durations, suggesting that the forces underlying buckling events are heterogeneous in magnitude, direction and/or points of application.

Simultaneous tracking of actively moving endosomes and microtubules

In the experiments presented so far, it is difficult, if not impossible, to determine which forces are acting on the MT. One solution would be to apply known forces to specific microtubules, for example, using a bead chemically bound to a cytoskeleton filament (Charlebois et al. 2010) or a microneedle to perturb the cell from the cortex (Brangwynne et al. 2007). However, these approaches are in some way artificial. Thus, we chose an alternative approach that minimally perturbs the system and at the same time allows us to observe the precise action of local forces in their physiological environment. We used fluorescent endosomes in combination with labeled microtubules (see "Materials and methods") and registered their motions. In privileged occasions we could witness clear and almost ideal events, such as the one observed in Fig. 6. From 170 movies we were able to clearly identify 45 events that linked MT buckling directly to the transported endosome. Some examples of these events are shown in movies ESM_4, ESM_5 and ESM_6.

Figure 6a shows some representative images of a cell region that also presented an endosome that was actively transported along a microtubule (see also, movie ESM_4). We followed the motion of two microtubules in this movie: the microtubule used as a track by the endosome (primary) and a second microtubule (secondary) that is crossing it (color lines in Fig. 6b). Figure 6a, b shows that both microtubules presented significant motion and shape variations during the studied time window (~60 s).

To obtain a broader view of the process, we generated an intensity matrix that shows the fluorescence of the primary microtubule on each frame (Fig. 6c). Interestingly, the green-channel intensity (which mostly represents the primary microtubule fluorescence) is not homogeneous, probably reflecting small, local variations in the concentration of XTP-EGFP attached to it. In this particular example, the green channel matrix showed regions of high intensity corresponding to the intersection between the tracked microtubules (arrowhead in Fig. 6a). We overlapped the intensity registered in the red channel to this matrix, corresponding to the endosome moving along the primary microtubule. It can be clearly observed that the secondary microtubule bends when the endosome passes over it (similarly to the condition shown in Fig. 1c). Figure 6a also shows that the primary microtubule buckles while the endosome is in contact with the secondary filament.

To correlate these buckling events with the motion of the endosome, we computed the buckling amplitude of both microtubules and the speed of the endosome in every frame, as described in "Materials and methods." Figure 6d shows that the amplitude of the secondary MT suddenly increased when the organelle reached the intersection as previously observed in the kymograph. Also, the organelle slowed down, suggesting that the intersecting microtubule acts as an elastic obstacle against the motors transporting the organelle. Simultaneously, the primary MT begins to bend as revealed by the slight amplitude increase until the endosome stalls completely when a sudden buckling event occurs. Finally, the endosome resumed its motion and both microtubules relaxed with similar time scales.

In the example shown in Fig. 6, the endosome slows down and pushes the transversal MT. At this point, we hypothesized that the motors transporting the endosome do not stop immediately after the encounter, but they continue stepping along the primary MT (Gittes et al. 1993). Since the endosome is trapped in the intersection, the motors push along the track, sliding this microtubule backwards.

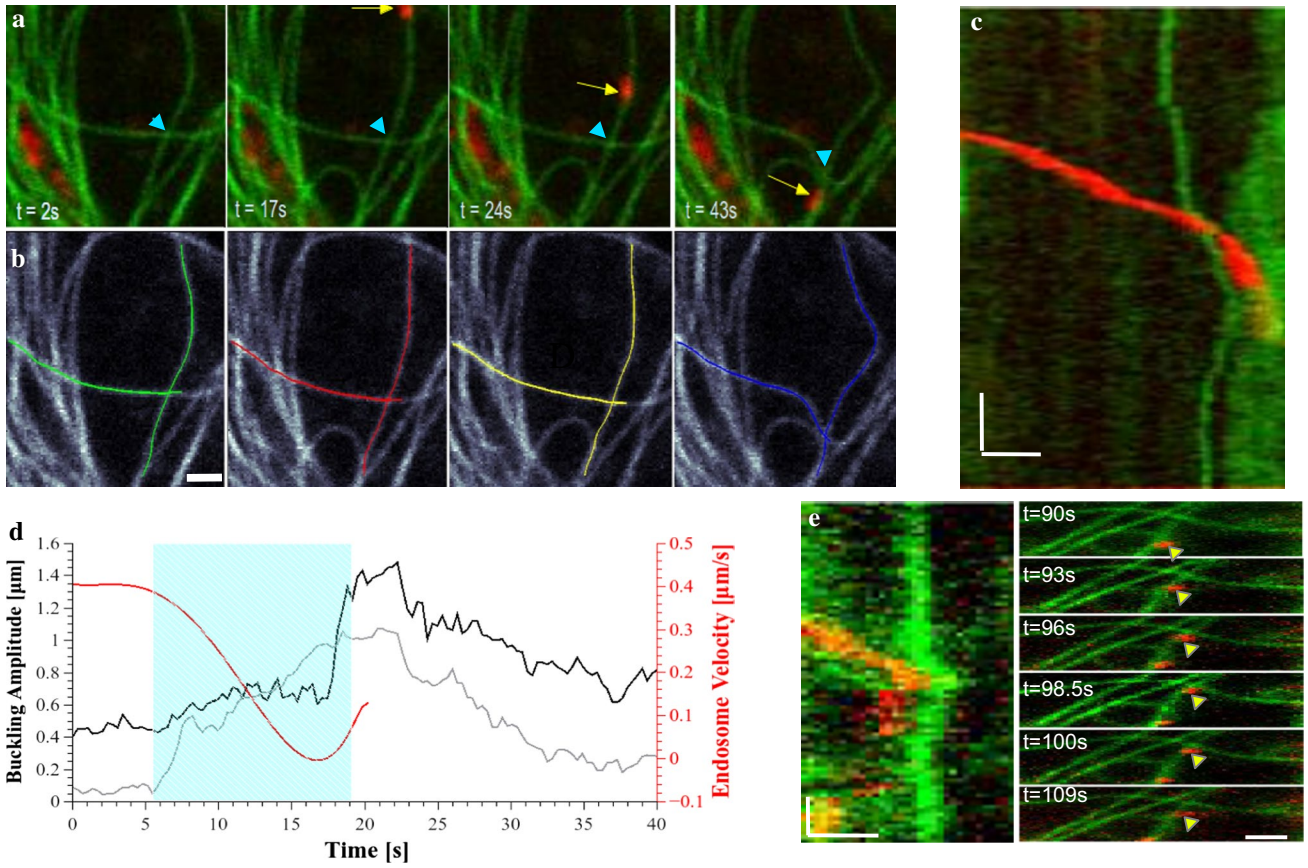

Fig. 6 Simultaneous tracking of fluorescent microtubules and endosomes. Buckling events and forces. **a** Pseudo-color superposition of two fluorescence channels in EGFP-XTP cells showing fluorescent MTs (*green*) and endosomes formed from endocytosis of FM 4-64 dye (*red*). Four non-consecutive frames are shown to illustrate filament shape fluctuations and endosome active transport. The *yellow arrow* indicates an endosome that is transported along a microtubule, and the *cyan arrowhead* indicates the MT intersection among the primary and secondary microtubule. **b** The same as in **a** but displaying only the *green channel* signal. Recovered shapes of two single filaments are shown. Note that the algorithm is robust under intersecting filaments. **c** Superposition of the two channels' fluorescence intensity matrices. *Each row* represents the fluorescence intensity along the coordinates of the filament upon which the endosome is being transported (*vertically oriented*). *Vertical scale bar* 5 s. *Horizontal scale bar* 1 µm. **d** Plot of the endosome velocity along the filament (*red*), the amplitude of the primary MT buckling (*black*) and of the secondary MT buckling (*gray*). The colored area (*cyan*) indicates the time while the endosome is in contact with the perpendicular filament. **e** Example of transported endosome reversing trajectory. Two-channel superposition kymograph, as shown in **c**. Time series of the two-channel microscopy are shown to illustrate significant events: transport, encounter, buckling, reverse transport. *Vertical scale bar* 52 s. *Horizontal scale bar* 1 µm

In other cases, the endosomes elastically deformed a crossing microtubule, but they were not able to pass over it and reversed their direction of motion (Fig. 6e; movie ESM_5) or they changed track (movie ESM_6).

We explored and analyzed 45 of these events, studying the relative orientation of the endosome track and the affected MT; 15 of them could be associated with sliding or tangential loads, while the rest revealed important transversal force components.

The examples shown in this section point toward the relevance of molecular motor forces in shaping microtubules in living cells. Microtubules constitute the main tracks for motor-driven organelles. However, they may also affect the transport in less direct ways; i.e., they can behave as obstacles in microtubule interceptions or they can push organelles during shape relaxation.

Discussion

Microtubules in living cells present transient, micrometer-sized deformations. To understand how these events form in the crowded cytoplasm and how long they persist, we studied microtubule buckling in living cells using *X. laevis* melanophores as a model system. In our experiments, EGFP-tagged XTP binds to microtubules, allowing their visualization. XTP is a microtubule-associated protein, homolog to tau protein (Olesen et al. 2002).

The influence of MAPs on the mechanical properties of microtubules is still not clear. While some authors demonstrated that different MAPs increased the flexural rigidity of purified microtubules (Felgner et al. 1996 and Mickey and Howard 1995), others reported an opposite effect (Portran et al. 2013). In a previous work, we studied the effect of EGFP-tagged XTP in live *X. laevis* melanophores and found no significant difference between the effective persistence length with control cells (Pallavicini et al. 2014), which implies that the flexural rigidity also is not significantly modified.

We tracked single fluorescent microtubules with nanometer precision and analyzed the dynamics of their deformations. We characterized their morphology by measuring buckling sizes, which were confined between 1 and 7 μm and developed amplitudes up to 4 μm. Buckling lengths were shorter than the MT length in the cell, suggesting that the filaments can transiently anchor at intermediate points, as proposed by Kent et al. (2016).

Buckling of these rigid cytoskeleton filaments requires active forces. To further assess this conclusion, we treated cells with sodium azide: neither relaxation of bent MTs nor new buckling arose. Also, the treatment with vinblatine—a drug that stabilizes MTs preventing depolymerization and polymerization processes—did not reduce the frequency of occurrence of bucklings, suggesting that polymerization forces, although they can contribute to the development of the MT curvatures typically observed in cells, are not the main source of compressive forces. These results reinforce previous works postulating that molecular motors bend MTs in living cells (Bicek et al. 2009; Wu et al. 2011; Kent et al. 2016).

Buckling events are characterized by a fast increase in the microtubule bending amplitude, followed by a relaxation process. After that, the microtubule typically recovers its initial shape. The average duration of the deformation was around 10 s. However, we observed rare events that lasted for a few minutes. We hypothesize that molecular motors, directly (i.e., by sliding microtubules) or indirectly (i.e., by a driven organelle) provide the load necessary to bend a microtubule; the force ends upon the motor release. Thus, the wide range of buckling durations can be understand considering the motor's force-dependent probability of detachment from the microtubule (Hendricks et al. 2012).

Microtubule buckling has also been proposed to influence cargo transport. Specifically, Kulic et al. (2008) observed buckling events associated with organelle transport, suggesting that the molecular motors that generate transport also provide the forces for these buckling events. Individual motor proteins exert forces of the order of a few piconewtons (pN) as measured in vitro (Schnitzer et al. 2000; Mallik et al. 2004). However, motors coordinate in teams within living cells generating larger forces (Soppina et al. 2009; Leidel et al. 2012). Using a two-color technique we were able to simultaneously track individual microtubules and endosomes in their natural environment. The correlation of the endosome active motion and the microtubule deformations revealed that the motor/s driving the endosome transport can generate local forces able to bend microtubules.

To further investigate the origin of the emergent features of microtubule buckling observed in living cells, we used a numerical approach. The model considered the effect of locally applied forces to a thin filament immersed in a viscous environment; the biophysical parameters were similar to those of the real system. The analysis of the filament shapes obtained with the numerical simulations allowed us to explain some of the experimental observations. First, we found that the amplitude of initially straight filaments grew exponentially at short times consistently with the buckling instability triggering (Howard 2001). On the other hand, the observation that some buckling events displayed a concave down amplitude time course for long times could be interpreted in terms of a constant compression or transverse load scenarios. In these cases, numerical simulations predict the attainance of a stationary shape compatible with a saturating amplitude.

The model proposed also considered the relaxation process occurring after the force release. We found that the characteristic times of the exponential decay of the amplitude during this process were in agreement with those obtained in the simulations.

Our results reinforce the picture of a transient spectrum of local forces randomly applied within the microtubule network and point toward the relevance of a molecular motor in shaping microtubules in living cells.

Materials and methods

Cell culture, sample preparation for imaging and confocal microscopy

The experiments in this article were done using a cell line of immortalized *X. laevis* melanophores stably expressing EGFP-tagged XTP, a *Xenopus* homolog of tau protein (Olesen et al. 2002; Levi et al. 2006). This cell line is a kind gift of Dr. Vladimir I. Gelfand (Northwestern University, Chicago, IL). The cells were cultured in 70% L-15 medium (Sigma-Aldrich, St. Louis, MO) supplemented with bovine fetal serum, as described in Rogers et al. (1997).

Phenylthiourea (PTU) was used to treat the melanophores to inhibit melanin production (Gross et al. 2002). Cells were grown for 2 days on sterilized 25-mm coverslips and placed onto 35-mm plates in 2 ml of complete medium for confocal microscopy measurements. Before

observation, the coverslips were washed in serum-free 70% L-15 medium (Sigma-Aldrich) and mounted in a custom-made chamber specially designed for the microscope.

For the vinblastine experiments, cells were treated with a 10 nM solution of vinblastine sulfate (Sigma-Aldrich) in PBS 70%. This concentration has been used previously to inhibit the microtubule polymerization-depolymerization dynamics without net depolymerization of the filaments (Robert et al. 2014). Cells were incubated for 30 min prior to imaging to assure arrest of microtubule dynamics. Control experiments without vinblastine were also performed. Wide-field fluorescence images of GFP-tagged microtubules were registered using an Olympus IX71 inverted microscope equipped with a 60× oil-immersion objective (numerical aperture 1.25), a U-MWIBA3 fluorescence filter cube (Olympus) and an excitation LED of 450 nm. Emitted light was collected by a QImaging EXi Aqua Bio-Imaging Microscopy Camera. Fields containing 4–5 cells were selected, and 200-frame movies were collected at a rate of 2 s/frame (400 s total time).

ATP depletion was carried out by incubating cells for 1 h in the presence of 50 mM deoxyglucose and 20 mM sodium azide before movie acquisition.

Fluorescent endosomes were generated by endocytosis of FM4-64 dye (Molecular Probes). Cells were treated with 4 μM FM4-64 dye in 70% L15 medium for 10 min prior to movie acquisition.

Confocal images were acquired in a model no. FV1000 confocal microscope (Olympus, Tokyo, Japan). A multiline Ar laser tuned at 488 nm (700 nW, average power at the sample) was used as the excitation source to observe EGFP fusion proteins. This excitation beam was reflected by a dichronic mirror and focused through an oil immersion UPlanSApo 60× objective (NA 1⁄4 1.35; Olympus) onto the sample. Fluorescence emission was collected by this objective as well, passed through a pinhole, reflected on a diffraction grating and passed through a slit set to transmit in the range of 500–600 nm. Finally, the fluorescence was detected by a photomultiplier set in the photon-counting detection mode. Images were acquired scanning the sample with this system at pixel times of 10–20 μs, and the pixel size was set in the range of 80–100 nm. For whole cell movies, the frame time ranged from 2–9 s, and for smaller regions of interest (ROIs) the temporal resolution was between 250 and 900 ms. The same set-up was used for fluorescent endosome experiments collecting red endosome fluorescence in a second emission channel in the range of 650–750 nm.

Microtubule localization and tracking

The acquired confocal movies were processed using a single-filament tracking routine AFTER (Pallavicini et al. 2014). With this algorithm, we recovered MT positions in living cells with sub-pixel resolution. For the signal-to-noise levels within living cells, the precision in the recovery of the filament position was approximately 10 nm.

AFTER requires the user to elect the desired filament to track and manually input initial coordinates for the first frame. Buckling MTs were selected observing the image sequences and tracked. In some cases complete buckling and relaxation events were studied, and in some only buckling or only relaxation was observed. Once the MT coordinates had been obtained, all the data were rotated and transported using MATLAB scripts to make the first and last y-coordinates equal to zero. In this way we could asses buckling amplitudes directly.

The amplitude of the deformation as a function of time was computed from the recovered shapes as the maximum y coordinate, in absolute value, since the direction of the buckling has no influence on our analysis.

The initial equilibrium and final times of the buckling events were determined from observation of the MT amplitude time evolution. This procedure was performed by eye inspection, as suggested in Fig. 5a, the initial buckling time was determined by the first moment when the amplitude presented a positive persistent derivative in time, and the duration of this growth was defined as buckling time. Amplitude variations >200 nm were considered buckling events. Finally, the time interval during which the amplitude decreased was defined as the relaxation time, and the instant when the variation began to flatten or returned to a growth period we defined the final buckling time.

Microtubule curvatures were calculated with the method proposed by Bicek et al. (2007). Briefly, we take three consecutive points from the filament tracking and compute the change in the angle (φ_k) and divide this by the average arc length of the two adjacent segments resulting in:

$$\kappa_k = \left| \frac{2\varphi_k}{\Delta s_{k+1} + \Delta s_k} \right| \tag{10}$$

which is an approximation of the curvature of small angle changes and small bond lengths. We repeat this procedure for all the positions along each filament and obtain the filament average curvature by computing the mean of all the individual curvatures: $\kappa = \langle \kappa_k \rangle$.

The speed of the endosome along the MT track was obtained as:

$$v_e = \frac{\Delta l}{\Delta t} \tag{11}$$

where Δl is the distance between successive positions, and Δt is the time interval between frames. We used the AFTER routine to track the position of the endosome on the microtubule from the kymograph (red channel in Fig. 6c). The tracked position was obtained with the

expected resolution, yet there were slight fluctuations from frame to frame, which rendered the recovered velocity with a very high noise level. To obtain a smoother velocity curve, we fitted the tracked positions to a polynomial and re-calculated Δl, which resulted in a better curve, which was representative of the endosome's velocity.

Numerical simulations

To understand the different possible scenarios on the microtubules, we used a worm-like chain model (Gauger and Stark 2006), which is the discretization of a continuum slender beam, which can be stretched and bent. The continuum potential energy is $V = V_{\mathrm{E}} + V_{\mathrm{B}}$, composed of elastic and bending terms

$$V_{\mathrm{E}} = \frac{1}{2} EA \int_0^L \left[|r'(l)| - 1 \right]^2 \mathrm{d}l \tag{12}$$

$$V_{\mathrm{B}} = \frac{1}{2} EI \int_0^L C^2(l) \left| r'(l) \right|^2 \mathrm{d}l \tag{13}$$

$$C(l) = \frac{\left| r'(l) \times r''(l) \right|}{|r'(l)|^3} \tag{14}$$

where C is the curvature, l is the longitudinal coordinate along the beam of total relaxed length L, and $r(l)$ is the position in space of the neutral axis. Discretization of the beam in N segments of length $\Delta l = L/N$ or $(N + 1)$ beads gives a potential energy depending on $(N + 1)$ independent coordinates r_n

$$V_{\mathrm{E}} = \frac{1}{2} \frac{EA}{\Delta l} \sum_{n=0}^{N-1} \left[\, |r_{n+1} - r_n| - \Delta l \, \right]^2 \tag{15}$$

$$V_{\mathrm{B}} = \frac{EI}{\Delta l} \sum_{n=1}^{N-1} \left[1 - \frac{(r_{n+1} - r_n)(r_n - r_{n-1})}{|r_{n+1} - r_n| \quad |r_n - r_{n-1}|} \right] \tag{16}$$

From these potential energies, deriving with respect to coordinates r_n, we obtain an elastic and bending force on each bead, respectively. We also took into account the viscous force, which is proportional to the velocity

$$F_n^{\mathrm{vis}} = -c \Delta l \, \dot{r}_n \tag{17}$$

where c is the viscous drag coefficient per unit length. For of a long cylinder, the viscous drag coefficient in the perpendicular and longitudinal directions is on the same order of magnitude. In our simulations, we took (Howard 2001):

$$c = \frac{4\pi\eta}{\log(L/\Theta) + 0.84} \tag{18}$$

with η and Θ, the viscosity and filament diameter, respectively. When an external force is applied, the total force on each bead can be computed. Thus, we have equations of motion that we integrate numerically to obtain the time evolution, neglecting the inertial term (overdamped regime).

In our simulations, we restrained the motion of the filament to a plane, because from the experiments it is not possible to obtain accurate information on the out of plane motion. We used the following parameters for microtubules: external diameter $\Theta = 25$ nm; flexural rigidity $EI = 2 \times 10^7$ pN nm^2 (Gittes et al. 1993); elastic constant $EA = 10^5$ pN (Howard 2001). We estimate the viscosity of the cytoplasm around 5000 times of water, so $\eta = 5 \times 10^{-6}$ pN s/nm^2. For simplicity, we performed all simulations for microtubules of 5000 nm length (except for Fig. 2b where the length dependence was analyzed), divided into $N = 50$ segments of 100 nm.

For the tangential load cases, the filament is fixed at one end (right), and a compressive force, F, is applied in the horizontal direction at the other. Clamped boundary conditions in both ends were considered (except in Fig. 2a where different boundary conditions were analyzed). Simulations are carried out for initial amplitudes $A_i = 0.1$ and $A_i = 500$ nm. For the constant force simulation $F = 36$, 40, 44 and 48 pN (the case with $F = 40$ pN is reported in this work) and for the constant velocity F is such that the moving end maintains a constant velocity $v = 100$, 50 and 10 nm/s in the horizontal direction (the fastest case is shown). Simulations with different forces and velocities were performed; the simulated filament shape evolutions are shown in Supplementary Figs. 7 and 8. For the lateral force scenario, both ends were embedded in the horizontal axis: free to move horizontally but not vertically, and a constant pushing force is applied at the center of the filament in the vertical direction. The simulations were performed for $F_1 = 8$, $F_2 = 16$ and $F_3 = 32$ pN, and all initial conditions are straight ($A_i = 0$).

Acknowledgements We are grateful to E. Cerda for fruitful discussions. We acknowledge support from the Agencia Nacional de Promoción Científica y Tecnológica (PICT 2012-0899) and Universidad de Buenos Aires (UBACyT 20020110100074, 20020120200244), Argentina. We also thank Dr. Vladimir I. Gelfand (Northwestern University, Chicago, IL) for providing the cell line used in this work.

References

Akhmanova A, Steinmetz MO (2015) Control of microtubule organization and dynamics: two ends in the limelight. Nat Rev Mol Cell Biol 16(12):711–726

Bicek AD, Tüzel E, Kroll DM, Odde DJ (2007) Analysis of microtubule curvature. Methods Cell Biol 83:237–268

Bicek AD, Tuzel E, Demtchouk A, Uppalapati M, Hancock WO, Kroll DM, Odde DJ (2009) Anterograde microtubule transport drives microtubule bending in LLC-PK1 epithelial cells. Mol Biol Cell 20(12):2943–2953

Brangwynne CP, MacKintosh FC, Kumar S, Geisse NA, Talbot J, Mahadevan L, Parker KK, Ingber DE, Weitz DA (2006) Microtubules can bear enhanced compressive loads in living cells because of lateral reinforcement. J Cell Biol 173(5):733–741

Brangwynne CP, MacKintosh FC, Weitz DA (2007) Force fluctuations and polymerization dynamics of intracellular microtubules. Proc Natl Acad Sci USA 104(41):16128–16133

Brangwynne CP, Koenderink GH, Mackintosh FC, Weitz DA (2008) Nonequilibrium microtubule fluctuations in a model cytoskeleton. Phys Rev Lett 100(11):118104

Charlebois BD, Schek HT 3rd, Hunt AJ (2010) Nanometer-resolution microtubule polymerization assays using optical tweezers and microfabricated barriers. Methods Cell Biol 95:207–219

Chernick MR (2007) Bootstrap methods: a guide for practitioners and researchers, 2nd edn

Dogterom M, Yurke B (1997) Measurement of the force–velocity relation for growing microtubules. Science 278(5339):856–860

Felgner H, Frank R, Schliwa M (1996) Flexural rigidity of microtubules measured with the use of optical tweezers. J Cell Sci 109(Pt 2):509–516

Fletcher DA, Mullins RD (2010) Cell mechanics and the cytoskeleton. Nature 463(7280):485–492

Gardel ML, Kasza KE, Brangwynne CP, Liu J, Weitz DA (2008) Mechanical response of cytoskeletal networks. Methods Cell Biol 89:487–519

Gauger E, Stark H (2006) Numerical study of a microscopic artificial swimmer. Phys Rev E Stat Nonlinear Soft Matter Phys 74(2 Pt 1):021907

Gittes F, Mickey B, Nettleton J, Howard J (1993) Flexural rigidity of microtubules and actin filaments measured from thermal fluctuations in shape. J Cell Biol 120(4):923–934

Gittes F, Meyhofer E, Baek S, Howard J (1996) Directional loading of the kinesin motor molecule as it buckles a microtubule. Biophys J 70(1):418–429

Gross SP, Tuma MC, Deacon SW, Serpinskaya AS, Reilein AR, Gelfand VI (2002) Interactions and regulation of molecular motors in *Xenopus* melanophores. J Cell Biol 156(5):855–865

Hendricks AG, Holzbaur EL, Goldman YE (2012) Force measurements on cargoes in living cells reveal collective dynamics of microtubule motors. Proc Natl Acad Sci USA 109(45):18447–18452

Howard J (2001) Mechanics of motor proteins and the cytoskeleton. Sinauer Associates, Inc, Sunderland

Howard J (2006) Elastic and damping forces generated by confined arrays of dynamic microtubules. Phys Biol 3(1):54–66

Howard J (2009) Mechanical signaling in networks of motor and cytoskeletal proteins. Annu Rev Biophys 38:217–234

Jin MZ, Ru CQ (2013) Localized buckling of a microtubule surrounded by randomly distributed cross linkers. Phys Rev E 88:012701

Kabir AMR, Inoue D, Afrin T, Mayama H, Sada K, Kakugo A (2015) Buckling of microtubules on a 2D elastic medium. Sci Rep 5:17222

Kent IA, Rane PS, Dickinson RB, Ladd AJ, Lele TP (2016) Transient pinning and pulling: a mechanism for bending microtubules. PLoS One 11(3):e0151322

Kimura A, Onami S (2005) Computer simulations and image processing reveal length-dependent pulling force as the primary mechanism for *C. elegans* male pronuclear migration. Dev Cell 8(5):765–775

Kulic IM, Brown AE, Kim H, Kural C, Blehm B, Selvin PR, Nelson PC, Gelfand VI (2008) The role of microtubule movement in bidirectional organelle transport. Proc Natl Acad Sci USA 105(29):10011–10016

Leidel C, Longoria RA, Gutierrez FM, Schubeita GT (2012) Measuring molecular motor forces in vivo: implications for tug-of-war models of bidirectional transport. Biophys J 103(3):492–500

Levi V, Serpinskaya AS, Gratton E, Gelfand V (2006) Organelle transport along microtubules in Xenopus melanophores: evidence for cooperation between multiple motors. Biophys J 90(1):318–327

Mallik R, Carter BC, Lex SA, King SJ, Gross SP (2004) Cytoplasmic dynein functions as a gear in response to load. Nature 427:649–652

Mickey B, Howard J (1995) Rigidity of microtubules is increased by stabilizing agents. J Cell Biol 130(4):909–917

Newman MEJ (2005) Power laws, Pareto distributions and Zipf's law. Contemp Phys 46(5):28

Nicastro D, Schwartz C, Pierson J, Gaudette R, Porter ME, McIntosh JR (2006) The molecular architecture of axonemes revealed by cryoelectron tomography. Science 313(5789):944–948

Olesen OF, Kawabata-Fukui H, Yoshizato K, Noro N (2002) Molecular cloning of XTP, a tau-like microtubule-associated protein from *Xenopus laevis* tadpoles. Gene 283(1–2):299–309

Pallavicini C, Levi V, Wetzler DE, Angiolini JF, Benseñor L, Desposito MA, Bruno L (2014) Lateral motion and bending of microtubules studied with a new single-filament tracking routine in living cells. Biophys J 106(12):2625–2635

Paluch EK, Nelson CM, Biais N, Fabry B, Moeller J, Pruitt BL, Kudryasheva G, Rehfeldt F, Federle W (2015) Mechanotransduction: use the force(s). BMC Biol 13:47. doi:10.1186/s12915-015-0150-4

Portran D, Zoccoler M, Gaillard J, Stoppin-Mellet V, Neumann E, Arnal I, Martiel JL, Vantard M (2013) MAP65/Ase1 promote microtubule flexibility. Mol Biol Cell 24(12):1964–1973

Rauch P, Heine P, Goettgens B, Käs JA (2013) Forces from the rear: deformed microtubules in neuronal growth cones influence retrograde flow and advancement. New J Phys 15:015007

Robert A, Herrmann H, Davidson MW, Gelfand VI (2014) Microtubule-dependent transport of vimentin filament precursors is regulated by actin and by the concerted action of Rho- and p21-activated kinases. FASEB J 28(7):2879–2890

Rogers SL, Tint IS, Fanapour PC, Gelfand VI (1997) Regulated bidirectional motility of melanophore pigment granules along microtubules in vitro. Proc Natl Acad Sci USA 94(8):3720–3725

Schnitzer MJ, Visscher K, Block SM (2000) Force production by single kinesin motors. Nat Cell Biol 2(10):718–723

Shekhar N, Neelam S, Wu J, Ladd AJ, Dickinson RB, Lele TP (2013) Fluctuating motor forces bend growing microtubules. Cell Mol Bioeng 6(2):120–129

Soppina V, Rai AK, Ramaiya AJ, Barak P, Mallik R (2009) Tug-of-war between dissimilar teams of microtubule motors regulates transport and fission of endosomes. Proc Natl Acad Sci USA 106(46):19381–19386

Walczak CE, Heald R (2008) Mechanisms of mitotic spindle assembly and function. Int Rev Cytol 265:111–158

Wu J, Misra G, Russell RJ, Ladd AJ, Lele TP, Dickinson RB (2011) Effects of dynein on microtubule mechanics and centrosome positioning. Mol Biol Cell 22(24):4834–4841

Yamada S, Wirtz D, Kuo SC (2000) Mechanics of living cells measured by laser tracking microrheology. Biophys J 78(4):1736–1747